Surface Review and Letters, Vol. 15, No. 6 (2008) 867–879

World Scientific
www.worldscientific.com

SURFACE PLASMON POLARITON LOCALIZATION

VICTOR COELLO
Centro de Investigación Científica y de Educación Superior de Ensenada, Unidad Monterrey, Alianza Sur No. 105, Nueva Carretera Aeropuerto Km 9.5 Parque de Investigación e Innovación Tecnológica (PIIT), Monterrey, N. L. Mexico C. P. 66629, Mexico
vcoello@cicese.mx

Received 21 March 2008

Localization of surface plasmons polariton is reviewed in the context of experiments and modeling of near-field optical images. Near-field imaging of elastic (in-plane) surface plasmon scattering is discussed, and approaches for the correct image interpretation are outlined. Nonlinear effects related to localized surface plasmons are pressented. Surface plasmon localization opens up numerous possibilities for application in biosensing, nanophotonics, and in general in the area of surface optics properties.

Keywords: Surface plasmon localization; surface waves; light localization.

1. Introduction

Localization of surface plasmon polaritons (SPPs)[1] remains as one of the most exciting studies related to SPP scattering by random surface nanostructures. Some examples of practical applications, in this context, are high-density optical data storage, contrast enhancement in local spectroscopy, and second-harmonic (SH) generation. Generally speaking, localization of light[2] is a phenomenon entirely originated due to coherent (in-plane) multiple scattering and interference in a random media. Light localization will occur if the mean free path becomes smaller or on the order of $\lambda/2\pi$, where λ represents the light wavelength. The effect was conceived on basis of two important developments in the well-known phenomenon of electron localization (Anderson localization): (1) the electron localization idea was phrased as an interference effect in multiple scattering and (2) a new phenomenon was observed, which was called weak localization. Thus, due to the fact that SPPs represent (quasi) two-dimensional waves, these electromagnetic modes may be used to observe localization phenomena (parallel to the metal surface) as a consequence of the strong scattering that an SPP undergoes in a surface with a relatively large roughness.[1] Actually, as an SPP field is strongly confined in the direction perpendicular to the surface, a direct observation of SPP localization is only possible by means of near-field optical microscopy techniques.[3] Imaging of SPPs with a scanning near-field optical microscope (SNOM) has clarified many features of SPP localization.[3] A serious problem to overcome, in those studies, is the nontrivial interpretation of the SPP field intensity distributions. This condition is partly originated because of the influence of propagating field components, generated due to the scattering of SPPs out of the surface plane, on the resultant near-field optical image. Such propagating waves are always present. However, it has been showed that the measurements can be accurate enough, if the near-field signal is mainly determined by the SPP field intensity distribution and the contribution of propagating waves is negligibly small.[4] Using such

criterions, near-field optical images of SPP optical fields along smooth metallic surfaces were recorded. They exhibited interference between the excited and scattered surface polaritons. The phenomenon was related to weak localization of SPPs caused by multiple scattering in the surface plane.[5,6] On the other hand, using rough gold surfaces, direct observation of SPP localization in the form of bright round spots with an enhancement ratio up to seven times the background signal was reported.[7,8] The position of such spots resulted to be angle dependent and not correlated to the surface topography. Even though an interesting progress in the understanding of SPP localization phenomena was achieved, there exists not at the moment a complete mathematical model to deal with that kind of studies. The scattering of SPP has been modeled by considering isotropic point-like scatterers whose responses to the incident SPP field are phenomenologically related to their effective polarizabilities.[8] As far as calculations are concerned, relatively straightforward simulations of SPP localization were reached. The simulations showed an overall appearance of the bright spots quiet similar to those ones experimentally observed in near-field optical images and that were attributed to strong SPP localization.[8] So far, it was clear from the outcome of the investigations that more systematic studies were needed. A different approach was a statistical study of the recorded near-field intensity distributions.[9] A systematic method was proposed in order to compare different samples and scattering configurations establishing information criteria beyond a qualitative observation of round bright spots. The SPP localization also plays a major role in surface enhancement phenomena as SH generation. In this context, round and bright spots ($\sim 10^3$ the background signal) were reported as a direct evidence of enhanced nanooptical fields (localized SPPs) generated via nonlinear interaction in metal nanostructures.[10]

Here, I present an overview of some of the problems, developments, and current progress related with our research in the surface polariton localization phenomena. I begin with an introduction to SPPs in Sec. 2 followed by a brief discussion of SNOM concepts in Sec. 3. Experimental results on weak and strong SPP localization will be presented in Secs. 4 and 5, respectively. Section 6 describes a multiple-scattering model that was used for simulation of SPP localization phenomena. A statistical treatment of near-field optical images that exhibited SPP localization will be analyzed in Sec. 7. Direct evidence of strong and spatially localized SH enhancement in random metal nanostructures is presented in Sec. 8. Finally, in Sec. 9, applications and further investigations of the SPP localization area are outlined.

2. Surface Plasmon Polaritons

SPPs are oscillations of surface electron charge density that can exist at a metal/dielectric interface (Fig. 1). Associated with them, there exists an electromagnetic field that propagates along the interface exhibiting exponential decays perpendicular to it. Therefore, SPPs show a high sensitivity to surface properties such as roughness and surface adsorbates.[1] As it is characteristic for evanescent fields,[11] for the SPP to exist, the wave number associated with it must be larger (in absolute value) than the light wave number in the neighbor media. Surface polaritons obey Maxwell's equations and they do represent (quasi) two-dimensional waves. The electromagnetic derivation of the SPP modes results in the fact that such modes are possible only for *p*-polarization of light (TM-waves), since *s*-polarized waves (TE) do not satisfy the boundary conditions. Owing to their electromagnetic nature, it is not difficult to infer that SPPs can diffract, reflect, and interfere. Those properties are clearly exhibited in the course of SPP scattering. Scattering of SPPs is usually caused by randomly placed surface imperfections (as even the most carefully prepared surfaces are not completely flat). Hereafter, we should distinguish between two kinds of SPP scattering: *inelastic and elastic SPP scattering.*

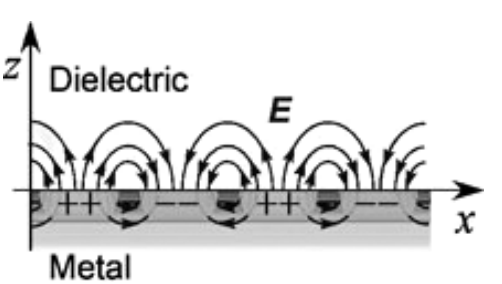

Fig. 1. Schematic representation of an SPP-field (E) that exists at a metal/dielectric interface (XZ plane).

For *inelastic scattering*, we will consider, propagating field components scattered away from the surface decreasing the total energy stored in SPPs. *Elastic scattering* occurs when SPPs are scattered by surface imperfections *along the surface plane*, i.e. into other SPPs preserving the total SPP energy. Concerning the mechanisms for SPP excitation, two techniques have been extensively developed: excitation by means of light and excitation by means of electrons. SPP excitation by electrons is beyond the scope of this work (an overview can be found in Ref. 1). Otto and Kretschmann configurations[1] are the mechanism most widely used for SPP excitation by light. They include a dielectric–metal–air system, in which a light beam is impinging on the metallic surface under an angle larger than the *critical angle*. The excitation occurs at the interface between air and metal and is recognized as a minimum in the angular dependence of the reflected beam power. An angular spectra analysis of SPP excitation allows one to deduce the SPPs characteristics, whose knowledge is indispensable for any kind of SPPs studies.

2.1. *Surface polaritons properties*

In order to show the SPP characteristics, first let us consider the interface between two semi-infinite media as air–metal. The SPP electric field existing in such a system (Fig. 1) can be represented as

$$E(x, y) = E_0 e^{i\beta\cdot\hat{x}} \cdot e^{-\gamma\cdot\hat{z}}, \tag{1}$$

which is an electromagnetic mode propagating in the x-direction along the surface and with an exponential decay perpendicular (z-direction) to it (Fig. 1). The SPP wave vector, β, and the air decay constant, γ, are derived through the use of Maxwell's equations and the boundary conditions, yielding the expressions

$$\beta = \frac{2\pi}{\gamma_0}\sqrt{\frac{\varepsilon_m}{1+\varepsilon_m}}, \quad \gamma = \sqrt{\beta^2 - k_0^2}, \tag{2}$$

with λ_0 being the incident wavelength, ε_m the dielectric constant of metal, and k_0 the incident wave number. The SPPs modes have an exponential decay into each of the media, γ_m, the SPP decay constant in the metallic medium is given by

$$\gamma_m = -\sqrt{\beta^2 - \varepsilon_m k_0^2}. \tag{3}$$

Other important SPP characteristics are, in turn, the *SPP wavelength*,

$$\Lambda_{\mathrm{SPP}} = \frac{2\pi}{\beta}, \tag{4}$$

the *propagation length*, i.e. the length at which the intensity decreases to $1/e$ (along the surface),

$$L_{\mathrm{SPP}} = \frac{1}{2\beta_{\mathrm{im}}}, \tag{5}$$

with β_{im} being the imaginary part of β, and *the penetration depth*, i.e. the length (perpendicular to the surface) at which the field amplitude decrease to $1/e$. It is given by

$$d_1 = \frac{1}{\gamma\ (\mathrm{air})}, \quad d_2 = \frac{1}{\gamma_m\ (\mathrm{metal})}. \tag{6}$$

3. Scanning Near-Field Optical Microscopy

In contrast with the traditional mechanism to measure SPP properties, SNOM techniques offer a direct way of probing an SPP field. The first proposal for such technique came from Synge in 1928.[12] Although not feasible with the technology at that time, his proposals form an accurate basis for the creation of a device for obtaining resolution beyond the Rayleigh–Abbe diffraction limit.[13] The operational principle involves illumination of a sample through a subwavelength sized aperture while keeping the aperture sample distance less than half of the illumination wavelength. Therefore, the light does not have the opportunity to diffract before it interacts with the sample, and the resolution does not depend on the wavelength but on the aperture diameter. The image is obtained by scanning the aperture along the sample and simultaneously recording its optical response with the help of conventional far-field detection techniques. Four decades afterwards, in 1972, the first experimental device with subwavelength resolution was reported.[14] The experiment was carried out in the microwave range ($\lambda \approx 3\,\mathrm{cm}$), reaching a resolution of $\lambda/60$. In 1984 and after a development of the necessary technology for experimental realization, Pohl and co-workers[15] showed the first SNOM imaging at visible wavelengths with a resolution of $\lambda/20$. The success of the new kind of imaging system instigated the advent of new configurations attempting to improve the technique as well as to adapt it to specifics needs (a review of SNOM configurations can

be found in Ref. 16). Nevertheless for all numerous SNOM versions, the fundamentals of this microscopy are found in the detection of evanescent fields.

4. SPP Weak Localization

Weak localization (or enhanced backscattering) is considered as a precursor of the effect of localization. It is also an interference effect in multiple scattering, but not as dramatic as strong localization. Weak localization arises from constructive interference (in the back scattering direction) between two waves scattered along the same path in opposite directions. Theoretical predictions of the SPP backscattering enhancement were reported about 3 ages ago.[17] In the experimental aspect, using a photon tunneling-SNOM[16,18] near-field optical images recorded at a relatively smooth silver surface (Fig. 2(a)) showed well-pronounced interference patterns (Fig. 2(b)). The phenomenon was reported as a direct evidence of SPP weak localization.

Topographical images taken at a different surface area for such a silver film showed a smooth surface with rarely spaced bumps in the central region (Fig. 3(a)). The corresponding near-field optical images were recorded, separately, at two excitation wavelengths (633 and 594 nm) and also exhibited very well-pronounced interference patterns (Figs. 3(b) and 3(c)).

Wavelength dispersion was noticeable in those images. This indicates that, in the central part of that film, scatterers are situated far away from each other, so that the regime of single SPP scattering still takes place in that region.

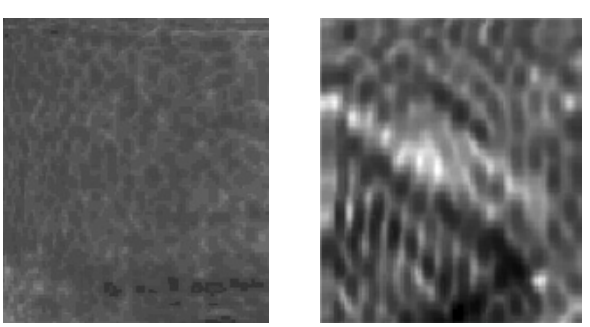

(a) (b)

Fig. 2. Gray-scale topographical (a) and near-field optical (b) images of $2.0 \times 2.5\,\mu\text{m}^2$ taken at the same place of the smooth silver film. The maximum height surface roughness in the topographical image (a) is 11 nm. The optical image is presented in a scale corresponding to $\sim$250–550 pW (b) of the detected optical signal.

(a) (b) (c)

Fig. 3. Gray-scale topographical (a) and near-field optical images (b, c) of $4.5 \times 3.6\,\mu\text{m}^2$ obtained at a rough region of the silver film for two wavelengths: 594 nm (b) and 633 nm (c). The maximum height surface roughness in the topographical image is 92 nm (a). Contrast of the optical images is $\sim$95%.

5. SPP Strong Localization

SPP localization is difficult to achieve since even for rough films it is not an automatically obtained effect.[19,20] It is quite difficult to find media in which one can get short mean free paths. One cannot make the volume fraction of scatterers larger and larger, since this leads not only to elastic but also to inelastic SPP scattering, which may result that the optical signal will be dominated by propagating components. Apparently, to optimize the amount of scattering, it is necessarily a large volume of scatterers whose sizes should approximately correspond to the SPP wavelength, λ_{SPP}. Scatterers smaller (in size) than λ_{SPP} are necessary for the near-field interactions responsible of the SPP confinement whereas those bigger than λ_{SPP} would result in strong multiple scattering indispensable for the SPP localization to occur. Then, in order to observe strong localization, ideally one would like to have a medium that scatters light very strongly and preferably with negligible absorption. Under similar sample conditions like the ones just described above (Fig. 4(a)), direct observation of SPP localization, in the form of bright round spots, was obtained (Fig. 4(b)).

The metallic films were fabricated by means of thermal evaporation technique. The rough gold films were evaporated on the base of a glass prism, which had previously been covered with a sublayer of colloidal gold particles (diameter $\sim$40 nm) dried up in atmosphere. Therefore, the introduced surface roughness was randomly distributed along the sample surface. SPPs were resonantly excited by means

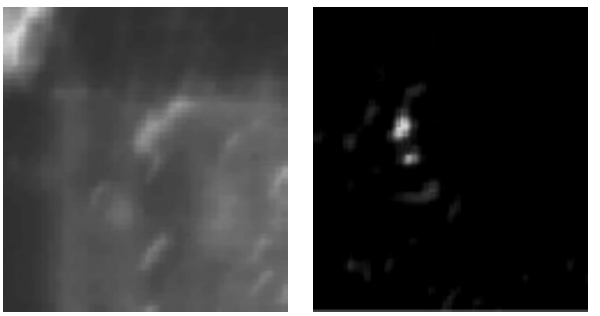

(a) (b)

Fig. 4. Gray-scale topographical (a) and near-field optical (b) images of $4.5 \times 3.6\,\mu m^2$ obtained with the gold film. The maximum height surface roughness in the topographical image is ~ 42 nm. Contrast of the optical images is $\sim 98\%$.

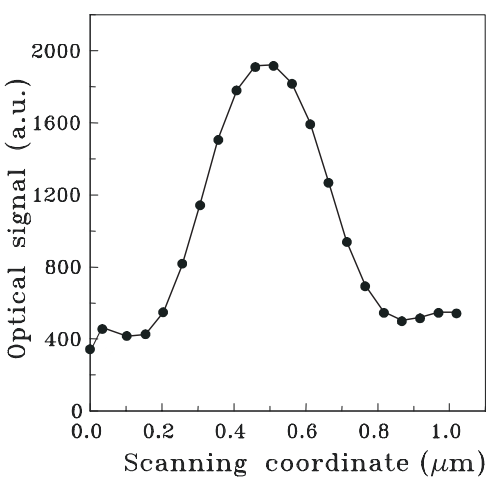

Fig. 5. Horizontal cross section of the near-field optical image of the bigger bright spot shown in Fig. 4(b).

of the Kretschmann configuration. The position of such spots resulted to be angle dependent and not correlated to surface topography. The size of the bright spots was estimated at ~ 300–400 nm (Fig. 5). The observations were directly related to the phenomenon of strong SPP localization,[4,19] which exhibited an enhancement ratio up to five times the background signal (Fig. 5).

6. Modeling of SPP Multiple Scattering

Typically, elastic scattering of SPP and the phenomenon of SPP localization were studied by direct evaluation of the near-field optical image obtained at the place where the SPP is being resonantly excited.[3] In general, this direction of SPP investigations has revealed several features that still have to be elucidated such as the necessary conditions to fulfill in order to obtain SPP localization. One could gain more understanding, in this context, investigating several configurations (e.g. varying the size and number of individual scatterers) of a particular sample. This task could be well complemented by means of numerical simulations. For instance, a scalar multiple-scattering approach was used for simulations of SPP strong interference conditions that may result in SPP localization.[4,8] Such model is based on two assumptions:

1. The elastic SPP scattering is dominant with respect to the inelastic scattering;
2. The SPP scattered by each scatterer represents an isotropic cylindrical SPP.

These assumptions allows one to avoid some of the complicated mathematical treatments involved in the problem of SPP scattering by surface inhomogeneities.[21] Then the field at a point in the plane pointed at by the vector $\mathbf{r}$ is given by

$$E(\mathbf{r}) = E_0(\mathbf{r}) + \sum_{j=1}^{N} \alpha_j E(\mathbf{r}_j) G(\mathbf{r}, \mathbf{r}_j), \qquad (7)$$

where $E_0(\mathbf{r})$ is the incident field, α_j is the effective polarizability of the jth dipole, $E(\mathbf{r}_j)$ is the self-consistent field at the site of the jth dipole, and $G(\mathbf{r}, \mathbf{r}_j)$ is the field propagator describing the scattered propagation of the scattered field from the jth dipole located at the source point $\mathbf{r}_j$ to the observation point $\mathbf{r}$. The self-consistent field to each dipole $E(\mathbf{r}_j)$ can be determined as

$$E(\mathbf{r}_j) = E_0(\mathbf{r}_j) + \sum_{l=1, l\neq j}^{N} \alpha_l E(\mathbf{r}_1) G(\mathbf{r}_j, \mathbf{r}_1). \qquad (8)$$

The total field at the site of the dipole j is the incoming field at the site of the scatterer and the sum of the scattered fields from all dipoles surrounding dipole j. The field in Eq. (8) then has to be inserted in Eq. (7) to find the total field at a point in the plane. The field propagator is given as

$$G(\mathbf{r}, \mathbf{r}_j) = \frac{i}{4} H_0^{(1)}(\beta |\mathbf{r} - \mathbf{r}_j|), \qquad (9)$$

where $H_0^{(1)}$ is the zero*th*-order Hankel function of first kind and β is the propagation constant for the

SPPs given by Eq. (2). The Hankel function first kind of order n is defined as

$$\begin{aligned} H_n^{(1)}(\beta|\mathbf{r}-\mathbf{r}_j|) &= J_n(\beta|\mathbf{r}-\mathbf{r}_j|) + iY_n(\beta|\mathbf{r}-\mathbf{r}_j|) \\ &= J_n(\beta|\mathbf{r}-\mathbf{r}_j|) \\ &\quad + i\frac{J_n(\beta|\mathbf{r}-\mathbf{r}_j|\cos(n\pi) - J_n(\beta|\mathbf{r}-\mathbf{r}_j|)}{\sin(n\pi)} \end{aligned} \tag{10}$$

where $J_n(\beta|\mathbf{r}-\mathbf{r}_j|)$ is the Bessel function of the first kind and, $Y_n(\beta|\mathbf{r}-\mathbf{r}_j|)$ is the Bessel function of the second kind, and n is the order. Often it is appropriate and easier to use the far-field approximation for the Hankel function. The far-field corresponds to large values of the argument, and the far-field approximation reads for large arguments[22]:

$$H_0^{(1)}(\beta|\mathbf{r}-\mathbf{r}_j|) \approx \sqrt{\frac{2}{\pi}}e^{-i\frac{\pi}{4}}\frac{e^{i\beta|\mathbf{r}-\mathbf{r}_j|}}{\sqrt{\beta|\mathbf{r}-\mathbf{r}_j|}}. \tag{11}$$

6.1. *Single scattering*

Following with the model, the SPP propagation was simulated by using a light wavelength $\lambda = 633\,\text{nm}$ in a silver film of 45 nm thickness whose dielectric constant had a typical value for such film of $\varepsilon = -16 + i$. The solution for the self-consistent field $\mathbf{E}(\mathbf{r}_j)$ (at the site of the scatterers) depends on the significance of the multiple scattering. That is to say, the significance of the multiple scattering is considered in relation with the ratio between the SPP propagation length, L, and the elastic scattering mean free path $l \sim R^2/\sigma$, where R is the average separation between scatterers and σ is the effective scattering cross section. That cross section is calculated by using the far-field approximation for the Hankel function (Eq. (11)), thus $\sigma = \alpha^2/[4Re(\beta)]$. If $l > L$ the regime of multiple scattering reduces to the regime of single scattering, and, consequently, the zero*th*-order Born approximation can be used to evaluate the field at the sites of the scatterers, i.e.

$$E^0(\mathbf{r}_j) = E_0(\mathbf{r}_j) \text{ Single scattering.} \tag{12}$$

We have developed numerical simulations for a total area of $5 \times 5\,\mu\text{m}^2$. In such area, 50 point-like scatterers were randomly distributed and illuminated by an SPP propagating from left to right. The single scattering regime (when the zero*th* Born approximation is applied) is exhibited in the numerical simulations as an interference pattern formed by the incident plane wave and the scattered cylindrical waves (Fig. 6(a)). The spatial Fourier spectrum was calculated in the $5 \times 5\,\mu\text{m}^2$ area. The spectrum showed a pair of open circles with the radius corresponding to the SPP propagation constant β (Fig. 6(b)). Analysis of the Fourier spatial spectra of near-field optical images may result in a better understanding of a particular regime of SPP scattering. Such analysis was used in order to establish the presence of the SPP backscattering in an experimental near-field optical image where the corresponding interference pattern was apparently hidden.[5]

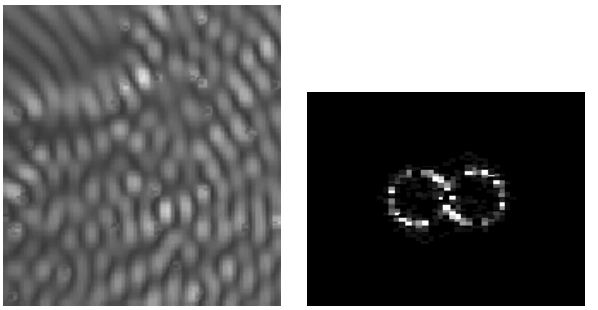

(a) (b)

Fig. 6. Gray-scale representations of the total field intensity distribution (a) and its corresponding Fourier spectra inside (b). The intensity distribution within the area of $5 \times 5\,\mu\text{m}^2$ was calculated in the regime of single scattering by 25 scatterers randomly distributed. Contrast of the images is 100%.

Here one should bear in mind that the Fourier spectrum $F(\boldsymbol{k})$ of an intensity distribution, which is a real function of spatial variables, has the Hermitian symmetry and, therefore, its magnitude distribution is symmetric with respect to the origin, i.e. $|F(-\boldsymbol{k})| = |F(\boldsymbol{k})|$. For example, the intensity interference pattern for two (unequal in amplitude) plane waves with wave vectors $\boldsymbol{k}_1$ and $\boldsymbol{k}_2$ would result in the Fourier spectrum, whose magnitude (besides being nonzero at $\boldsymbol{k} = 0$) has the same value for $\boldsymbol{k} = \pm(\boldsymbol{k}_2 - \boldsymbol{k}_1)$. Thus, the pair of open circles of Fig. 6(b) had a radio corresponding to the spatial frequency of $2\lambda/\lambda_{\text{SPP}}$. They originated due to interference between the excited SPP (travelling from left to right in the images) and SPP scattered in all possible directions.

6.2. *Multiple scattering*

If $L \gg l$, the regime of multiple SPP scattering prevails, and the successive Born iterations should be used to calculate the self-consistent field at the site of each scatterer:

$$E^n(\mathbf{r}_j) = E_0(\mathbf{r}_l) + \sum_{l=1, l\neq j}^{N} \alpha_j E^{n-1}(\mathbf{r}_l) G(\mathbf{r}_j, \mathbf{r}_l)$$

Multiple scattering. (13)

If the resonance interaction is rather strong, as it could be in the case of SPP strong localization, the Born iterations becomes divergent. In that case, the exact solution of the self-consistent equation (Eq. (8)) has to be employed. The corresponding numerical calculations showed that the Born series expansion rapidly converges, and only a few iterations (typically, $n < 10$ in Eq. (8)) were sufficient to obtain stable values of the self-consistent field at the sites of the scatterers. A numerical simulation of the intensity distributions of this scattering regime is presented in Fig. 7(a). The corresponding Fourier spectrum was diffuse (Fig. 7(b)) and contains notably more spatial frequencies than do the case of single scattering.

The spectrum showed a filled circle with the radius twice the propagation constant, which corresponds to a well-developed multiple scattering. One can also imagine rotation of the pair of open circles in Fig. 6(b) to produce the spectrum in Fig. 7(b). The wavelength influence, on the intensity distributions, was also numerically investigated for the multiple-scattering regime. In the case when the propagation length L is smaller than the lateral extension

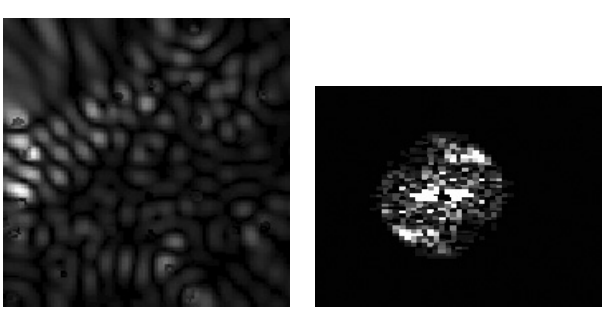

(a) (b)

Fig. 7. Gray-scale representation of the total field intensity distribution (a), which was calculated in the regime of multiple scattering, and its corresponding Fourier (b). All else is as in Fig. 6.

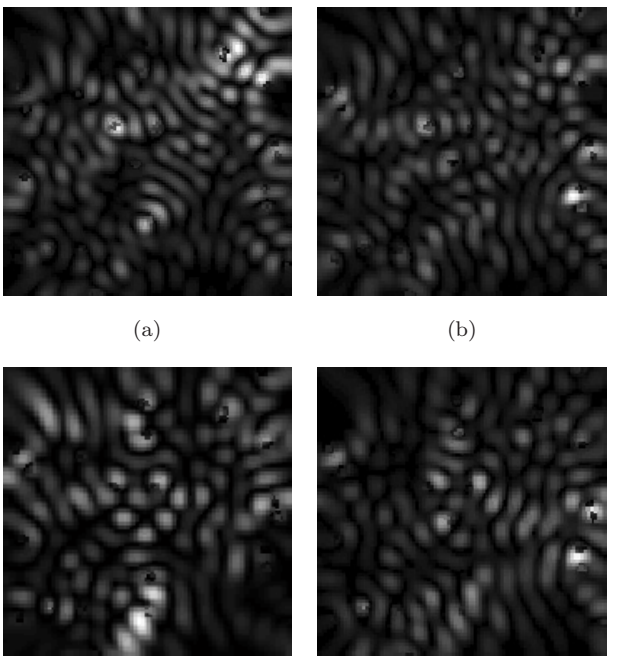

(a) (b) (c) (d)

Fig. 8. Gray-scale representations of the total field intensity distributions in an area of $5 \times 5\,\mu\text{m}^2$ calculated in the regime of multiple scattering by 25 scatterers randomly distributed in the area. The images were simulated for different wavelengths of light being (a) 570, (b) 600, (c) 630, and (d) 660 nm. Contrast of the images is 100%.

of the area of the scatterers, the corresponding interference pattern should change if the light wavelength is changed by $\delta\lambda \sim \lambda^2/L \sim 15\,\text{nm}$[8]. We developed numerical simulations (in an area noticeable smaller than L), where the wavelength was varied from 570 to 660 nm in the intervals of 30 nm (Figs. 8(a)–8(d)).

It was particularly with this wavelength variation (30 nm) where we could observe pronounced differences of the interference patterns calculated. Those changes were most obvious in the exchange of positions of the bright spots appearing on the calculated intensity distributions. In general, the numerical simulations had an overall appearance (Fig. 9(a)) and a signal enhancement (Fig. 9(b)) similar to those images experimentally observed[4,8,19] at a rough gold surface and which were attributed to strong SPP localization.

Despite the apparent success, the model presented limitations, one of them being that the effective polarizability of an individual scatterer is a phenomenological quantity, which is difficult to relate

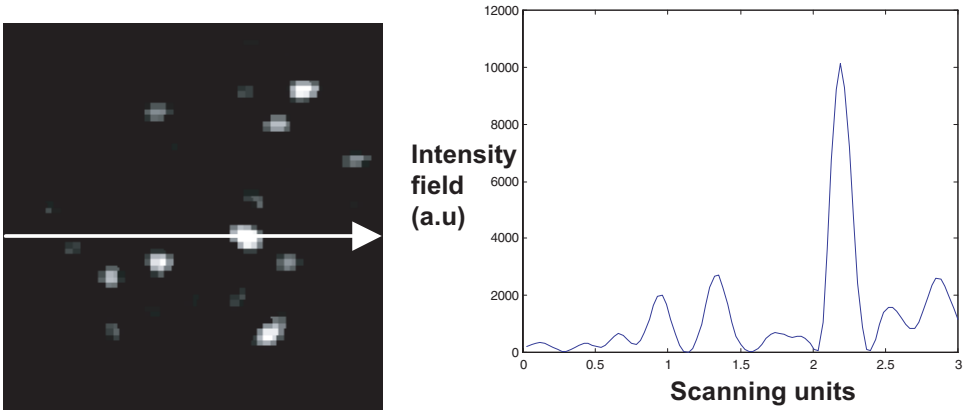

(a) (b)

Fig. 9. Gray-scale representation of the total field intensity distribution (a), which was calculated in the regime of multiple scattering. (b) The cross section of the near-field optical image of the bright spots shown in Fig. 9(a) (white arrow). All else is as in Fig. 6.

to scatterers parameters (e.g. size, dielectric susceptibility, etc.). Such an approach was extended into a vector dipolar multiple-scattering theory and used, among other things, to calculate SPP scattering produced by band-gap structures and an SPP interferometer.[23,24] This approach entails point-like dipolar scatterers interacting via SPPs so that the multiple-scattering problem in question can be explicitly formulated, making it very attractive for modeling of SPP phenomena. The validity of the model was established for relatively large inter-particle distances, whereas for smaller distances it was more accurate to use a total Green's tensor and include multipolar contributions in the scattered field (Ref. 23 and references therein). The self-consistent polarization of each scatterer established in the process of multiple scattering is obtained by solving the following equation:

$$P_i = \alpha_i \cdot \mathbf{E}^0(\mathbf{r}_i) + \frac{k_0^2}{\varepsilon_0} \sum_{n \neq i} \alpha_i \cdot G(\mathbf{r}_i, \mathbf{r}_n) \cdot P_n, \qquad (14)$$

where P_i is the polarization of the particle i, α is the polarizability tensor for particle i with the multiple scattering between the particle and the metal surface taken into account, E_0 is an incoming electric field, k_0 is the free space wave number, ε_0 is the vacuum permittivity, and $G(\mathbf{r}_i, \mathbf{r}_n)$ is the Green tensor for the reference structure (total field propagator). The Green tensor G is the sum of a direct contribution G_d, in this case the free space Green tensor, and an indirect contribution G_s that describes both reflection from the metal/dielectric interface and excitation of SPPs. The incoming E_0 describes a Gaussian SPP field impinging on the arrangement of scatterers. For a spherical particle made of the same metal as the substrate, the polarizability tensor is given by

$$\alpha \approx \left[\mathbf{I} - \frac{\varepsilon - 1}{\varepsilon + 1} \frac{\varepsilon - 1}{\varepsilon + 2} \left(\frac{1}{8} \hat{x}\hat{x} + \frac{1}{8} \hat{y}\hat{y} + \frac{1}{4} \hat{z}\hat{z} \right) \right]^{-1} \cdot \alpha^0, \qquad (15)$$

where $\mathbf{I}$ is the unit dyadic tensor, ε is the metal dielectric constant, $\hat{x}, \hat{y}, \hat{z}$ are unit vectors in a Cartesian coordinate system with $\hat{z}$ being perpendicular to the air–metal interface, and $\alpha^0 = \varepsilon_0 \mathbf{I} 4\pi a^3 \frac{\varepsilon - 1}{\varepsilon + 2}$ is the free space polarizability tensor in the longwave electrostatic approximation with α being the sphere radius. The polarizations (Eq. (1)) and the total field,

$$\mathbf{E}(\mathbf{r}) = \mathbf{E}^0(\mathbf{r}) + \frac{k_0^2}{\varepsilon_0} \sum_n \mathbf{G}(\mathbf{r}, \mathbf{r}_n) \cdot \mathbf{P}_n, \qquad (16)$$

can be calculated using the appropriate Green tensor for the reference structure $G(\mathbf{r}, \mathbf{r})$. Finally, based on the initial assumptions, it was proposed to use a three-dimensional dyadic Green tensor approximation, which accounts only for the SPP elastic scattering channel.[23] The complete analysis of the validity domain of such an approximation is beyond the scope of this work and can be found elsewhere.[23]

7. Statistical of SPP Localization Near-Field Images

A different approach, to the classical observation and analysis of hot spots, consisted of a statistical study of the recorded near-field optical images.[9] The main purpose of the approach was to evaluate a probability density function (PDF) for the total near-field intensity distributions in a specific scattering regime. The basis of the probability sampling was the selection of sampling units from the images with the same surface sample, excitation wavelength, and light polarization. Additionally, the recorded images were chosen with an overall appearance, as far as the image contrast is concerned, similar to each other. The average value of the detected signal in the selected images was adjusted to be the same, and the intensity range was then divided from 0 to a maximum intensity $I_{\max} = 1$. The procedure allows one to collect a sufficiently large number (typically, $> 10{,}000$) of data. That is to say, a significant collection of field intensities related to a particular scattering configuration. Once the intensity sampling was determined, it can be estimated the corresponding PDF. The PDF was approximated by a discrete distribution, whose values were evaluated at the intensity intervals $\Delta I = 0.04$ by counting the number of points n_k with intensities falling in the interval (I_k, I_{k+1}). Therefore, $\mathrm{PDF}(I_k) = n_k/(N\Delta I)$, where N is the total number of points. The resulted dependencies were plotted on the logarithmic scale for the probability and on the linear scale for the intensity. First, the PDF was evaluated for the near-field optical images reported as evidence of SPP weak localisation.[5] Those images were recorded at a light wavelength of 633 nm and using a smooth surface made of gold. One can see that the obtained PDF represents a symmetric distribution centered at the intensity of the resonantly excited SPP (Fig. 10).

The presence of the backscattered SPP, and other scattered SPPs, resulted in the interference pattern exhibiting approximately the same amount of larger (constructive interference) and smaller (destructive interference) intensities in comparison with the incident SPP intensity (Fig. 10). Apparently, one should expect such a PDF for the regime of single or weak multiple scattering with the scattered SPPs being weaker or close to the incident SPP. In the regime of well-developed multiple SPP scattering leading

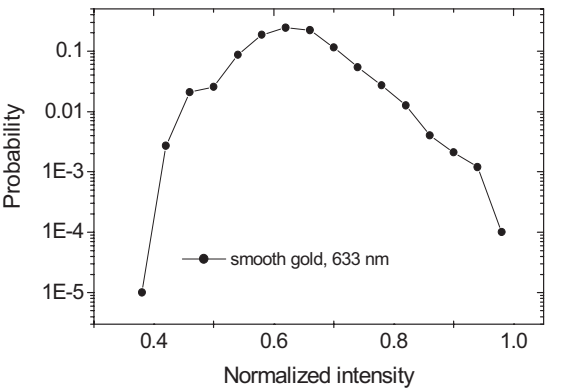

Fig. 10. Probability density function (PDF) of the normalized intensity obtained from near-field images exhibiting similar conditions to the one in Fig. 2(b). The PDF was plotted on the logarithmic scale.

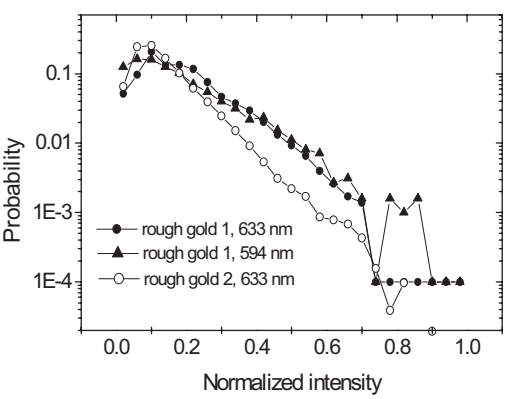

Fig. 11. Probability density functions (PDFs) of a sample population randomly obtained from near-field images similar to Fig. 4(b) using red (circles) and yellow (triangles) light. The PDFs were plotted on the logarithmic scale for the probability and on the linear scale for the intensity. The PDFs were obtained using two different sets of images named rough gold 1 (filled symbols) and rough gold 2 (open symbols).

to strong localization, the total scattering SPP field becomes dominant. Then the area with intensities stronger than the incident one is increased and, consequently, one should expect to obtain an asymmetric (positively skewed) PDF (Fig. 11). The same overall behavior of the PDF was obtained by using an additional set of images taken (at 633 nm) under similar experimental conditions but with a completely different rough gold film.[8] Note that similar PDFs were simulated for rough metal surfaces with large fractal dimensions.[25] Overall, it is clear that there exists a significant statistical difference between the

SPP intensity distributions established in different scattering regimes (at smooth and rough films).

8. SH Far-Field Microscopy of Localized SPPs

Novel optical phenomena arising from the propagation of SPPs at a weakly corrugated metal surface originated original contributions in the area of SPP-enhancement of SH diffraction.[10] The experimental setup (Fig. 12) used, for this kind of experiments, was a so-called SH scanning optical microscope (SHSOM).

It consisted of a scanning optical microscope in reflection geometry built on the base of a commercial microscope and a computer controlled two-dimensional (XY) translation stage. The XY stage is able of moving in steps down to 50 nm with the accuracy of 4 nm within a scanning area of $25 \times 25\,\mathrm{mm}^2$. A mode-locked pulsed Ti-Sapphire laser tunable was used in the range of 730–920 nm with pulse duration of ~ 200 fs, 80 MHz of repetition rate and an average output power of ~ 300 mW. The linearly polarized light beam from the laser is used as a source of sample illumination at the fundamental harmonic (FH) frequency. The laser beam passes through a wavelength selective splitter and it is focused at normal incidence on the sample surface (spot size $\sim 1\,\mu$m) with a Mitutoyo infinity-corrected long working distance $\times$ 100 objective. In order to avoid thermal damage on the sample, the average incident power was kept at the level of ~ 20 mW (intensity at the surface $\sim 2 \times 10^6\,\mathrm{W/cm}^2$). The sample reflects the FH and the generated SH radiation back to the same objective. The FH and SH signals are separated with the beam splitter and, after passing the appropriated filters and polarizers, detected with a photodiode and a photomultiplier tube, respectively. Finally both signals are recorded as a function of the scanning coordinate obtaining, simultaneously, FH and SH images of the sample surface. The resolution of the SHSOM was evaluated in $\sim 0.7\,\mu$m using domain walls of an electric field poled $KTiOPO_4$ quasi-phase matching crystal.[26] The sample under investigation was fabricated by using thermal evaporation and electron beam lithography techniques (more information about the procedure is found in Ref. 27). The final sample structure consists of high-density scattering regions composed of gold bumps (~ 70 nm high) randomly distributed over a thin (~ 50 nm) gold film. The scattering regions density is approximately 50 scatterers per $1\,\mu\mathrm{m}^2$ and contains $2\,\mu$m-wide channels free from scatterers that were used for investigations of guiding of SPPs.[27] There were recorded simultaneously FH and SH images of a dense scattering region in the wavelength range of 750–830 nm. The overall behavior of images of the same particular signal was very similar (Figs. 13(a)–13(f)). In general

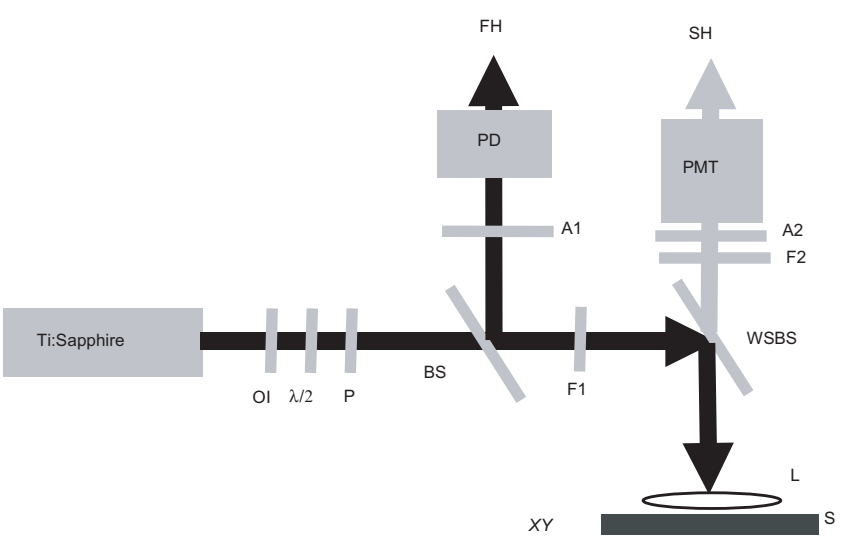

Fig. 12. Schematic of the experimental setup. OI: optical isolator, $\lambda/2$: half-wave plate, P: polarizer, BS: beam splitter, F1 and F2: filters, WSBS: wavelength selective beam splitter, L: objective, S: sample, XY: stage, A1 and A2: analyzers, PMT photomultiplier tube, and PD: photodiode.

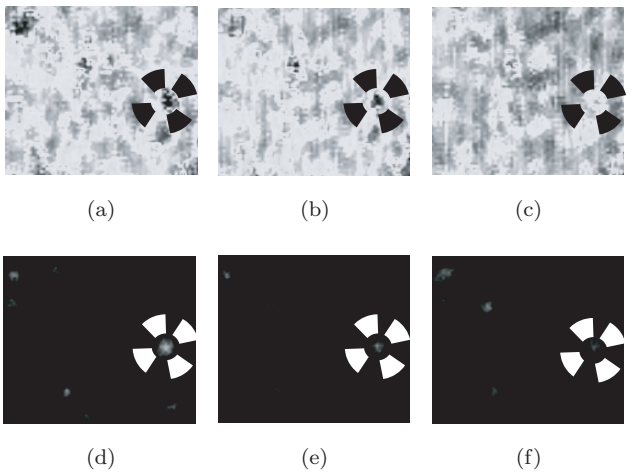

Fig. 13. Gray-scale FH (a)–(c) and corresponding SH (d)–(f) images of $8 \times 8\,\mu m^2$ obtained for 770 (a) and (d), 780 (b) and (e), and 790 (c) and (f) nm of the FH wavelength. The polarizations of the FH (incident) and the SH (detected) signal were both kept vertical with respect to the presented images, respectively. The maximum of the SH signal was 1200 cps (d). Representative dark (a)–(c) and bright (d)–(f) spots were enclosed in circles for better visualization.

one can appreciate bright and dark regions, which are a collection of small and round bright spots similar to those reported as evidence of localized SPPs.[4,7,8] The presence of the observed spots suggested that the total detected FH radiation can be considered as a superposition of the FH beam reflected from the flat gold surface and the FH field scattered by strongly interacting gold bumps. The latter contribution is related to the regime of multiple scattering of the light, which exhibits strong polarization and frequency dependence,[28] and can be expected to occur, for example, due to localization of resonant dipolar excitations at nanostructured surfaces. In general, one should expect the most efficient excitation for well-localized modes with one strong field maximum. Light scattering via excitation of such a mode (arising from the nanoparticles) should be similar to the dipole scattering resulting in the excitation of SPP modes. SPPs are scattered, in turn, in the surface plane and into the substrate as well as absorbed due to the internal damping. These processes contribute to the decrease of the total flux in the direction of reflection and, thereby, formation of dark spots (see spots enclosed in circles in Figs. 13(a)–13(c)). The images showed a noticeable re-distribution of the intensity. The bright spot (enclosed in circle) seen clearly in Fig. 13(d) was redistributed in Fig. 13(f). Taking this into account, one can claim that the bright spots were not correlated with surface defects since they show illumination wavelength dependence. It is also possible to notice that dark FH spots coincide with bright SH ones (enclosed spots in Figs. 13(a)–13(f)). About this fact, an explanation can be formulated. Excitation of an FH eigenmode (leading to the local FH enhancement) results in a strong SH signal only if the SH field, which is associated with the generated nonlinear polarization, is further enhanced due to excitation of the corresponding SH eigenmode. That is to say, FH and SH eigenmodes should overlap in the surface plane. However, in general, such a correspondence is very difficult to observe because of the relative low contrast of FH images.

9. Outlook

In this paper, the basic ideas of SPPs and the main experimental results concerning the phenomenon of SPP localization along with relevant numerical simulations were reviewed. As far as the SPP localization phenomenon is concerned, it should be stressed that there are many basic and technological aspects that have to be yet explored. The physics behind such a phenomenon is not simple. For instances, the influence of dissipation and wave–wave interaction are not clarified yet.[29] An enormous advance, in this context, was achieved with the advent of the SNOM techniques. Thus, features such as the influence of the inelastic scattering were elucidated. The use of numerical simulations of SPP scattering regimes was pointed out, and the relationship between scattering regime and spatial Fourier spectra of the field intensity distributions was investigated. The results were in agreement with the experimental observations presented here, and others reported elsewhere.[4,7,8] The localization studies were well complemented by making use of a statistical treatment of the recorded near-field optical images. It was established that there exists a significant statistical difference between the field intensity distributions established in different scattering regimes. On the other hand, we imaged a 50 nm gold nanostructured surface with an SHSOM in the wavelength range of 750–830 nm. FH and SH images showed wavelength dependences in their optical intensity distributions, which is in agreement

with the expected for multiple-scattering phenomena. Round and bright ($\sim 10^3$ the background signals) spots were observed in the SH images. The spots were attributed to the overlap in location and polarization of FH and SH eigenmodes in the surface plane. The overall behavior of the SH images was related as a *direct* evidence of enhanced nanooptical fields (localized SPPs) generated via nonlinear interaction in metal nanostructures.

In general, the SPP localization area is a very exciting field and many interesting results did not find their way into the above material. One of them being the SPP two-dimensional optics,[8,30–32] which is an excellent development for a local control of SPP propagation, in consequence, allows the possibility to obtain SPP localization in a controlled form. Additionally one can mention the full photonic band gaps for SPPs excited along periodically nanostructured surface, which opened exciting possibilities for SPP localization, since localization could be realized with a low disorder near an edge of a band gap.[33] The local control of SPP localization fields and consequent maximized efficiency of them should be further elucidated. Promising applications in this context can be found in nonlinear optical probing of molecules, nanomodification, and in general in nanoscience and nanotechnology.

Acknowledgments

This project was supported by CONACyT SEP-2004-C01-45999. The paper was substantially benefited with discussions and very helpful reviews of S. Bozhevolnyi, Jonas Beerman and B. Vohnsen.

References

1. H. Raether, *Surface Plasmons*, Springer Tracts in Modern Physics, Vol. 111 (Springer, Berlin, 1988); V. M. Agranovich and D. L. Mills (eds.), *Surface Polaritons* (North-Holland, Amsterdam, 1982).
2. *Photonics Crystals and Light Localization in the 21st Century*, C. M. Soukoulis (ed.), NATO Science Series, Series C Mathematical and Physical Science, Vol. 563 (Springer, Berlin, 2001).
3. *Near-Field Optics and Surface Plasmon Polaritons*, S. Kawata (ed.), Topics in Applied Physics, Vol. 81 (Springer, Berlin, 2001).
4. V. Coello, S. I. Bozhevolnyi and F. A. Pudonin, *Proc. SPIE* **3098** (1997) 536.
5. S. I. Bozhevolnyi, A. V. Zayats and B. Vohnsen, in *Optics at the Nanometer Scale*, eds. M. Nieto-Vesperinas and N. Garcia (Kluwer, Dordrecht, 1996).
6. K. M. Engenhardt and S. Gregory, *J. Opt. Soc. Am. B* **17** (2000) 593.
7. S. I. Bozhevolnyi, *Phys. Rev. B* **54** (1996) 8177.
8. S. I. Bozhvevolnyi and V. Coello, *Phys. Rev. B* **58** (1998) 10899.
9. V. Coello and S. I. Bozhevolnyi, *J. Microsc.* **202** (2001) 136; S. I. Bozhevolnyi and V. Coello, *Phys. Rev. B.* **64** (2001) 115414.
10. V. Coello, J. Beermann and S. Bozhevolnyi, *Phys. Stat. Sol. C* **8** (2003) 3070; S. I. Bozhevolnyi, J. Beermann and V. Coello, *Phys. Rev. Lett.* **90** (2003) 197403.
11. *Evanescent Waves from Newtonian Optics to Atomic Optics*, ed. F. de Fornel (Springer-Verlag, Berlin, 2001).
12. E. H. Synge, *Phil. Mag.* **6** (1928) 356.
13. L. Rayleigh, *Phil. Mag.* **42** (1896) 167; E. Abbe, *Arch. F. Mikroskop. Anat.* **9** (1873) 413.
14. E. Ash and G. Nicholls, *Nature* **237** (1972) 510.
15. D. W. Phol, W. Denk and M. Lanz, *Appl. Phys. Lett.* **44** (1984) 651.
16. *Near-Field Microscopy and Near-Field Optics*, ed. D. Courjon (Imperial College Press, World Scientific, 2003).
17. M. P. Van Albada, M. B. Van der Mark and A. Lagendijk, Experiments of weak localization of light and their interpretation, in *Scattering and Localization of Classical Waves in Random Media*, ed. P. Sheng (World Scientific, Singapore, 1990).
18. R. C. Reddick, R. J. Warmack and T. L. Ferrel, *Phys. Rev. B* **39** (1989) 767; D. Courjon, K. Sarayeddine and M. Spajer, *Opt. Commun.* **71** (1989) 23; F. de Fornel *et al.*, *Proc. SPIE* **1139** (1989) 77.
19. S. I. Bozhevolnyi, *Phys. Rev. B* **54** (1996) 8177.
20. A. A. Maradudin, I. Simonsen, T. A. Leskova and E. R. Méndez, *Phys. B Condens. Matt.* **296** (2001) 85.
21. A. V. Shchegrov, I. V. Novikov and A. A. Maradudin, *Phys. Rev. Lett.* **78** (1997) 4269.
22. M. Abramowitz and I. A. Stegun, *Handbook of Mathematical Functions*, 9th edn. (Dover, New York, 1972).
23. T. Søndergaard and S. I. Bozhevolnyi, *Phys. Rev. B* **67** (2003) 165405.
24. V. Coello, T. Søndergaard and S. Bozhevolnyi, *Opt. Commun.* **240** (2004) 345.
25. J. A. Sánchez-Gil and J. V. García-Ramos, *J. Chem. Phys.* **108** (1998) 317.
26. B. Vohnsen and S. I. Bozhevolnyi, *J. Microsc.* **202** (2001) 244.
27. S. I. Bozhevolnyi, V. S. Volkov and K. Leosson, *Phys. Rev. Lett.* **89** (2002) 186801.
28. S. I. Bozhevolnyi, in Optics of Nanostructured Materials, pp. 330–358, and references therein.

29. S. John, in *Scattering and Localization of Classical Waves in Random Media*, ed. P. Sheng (World Scientific, Singapore, 1990), p. 1.
30. S. I. Bozhevolnyi and F. A. Pudonin, *Phys. Rev. Lett.* **78** (1997) 2823.
31. I. I. Smolyaninov, D. L. Mazzoni, J. Mait and C. C. Davis, *Phys. Rev. B* **56** (1997) 1601.
32. W. L. Barnes, A. Dereux and T. W. Ebbesen, *Nature* **424** (2003) 824.
33. J. Qi and T. Rui-bao, *Phys. Rev. B* **43** (1991) 6136.